


# Shoreline dissipation of infragravity waves

A.T.M. de Bakker, M.F.S. Tissier, B.G. Ruessink

PII: S0278-4343(13)00378-6
DOI: http://dx.doi.org/10.1016/j.csr.2013.11.013
Reference: CSR2919

To appear in: *Continental Shelf Research*

Cite this article as: A.T.M. de Bakker, M.F.S. Tissier, B.G. Ruessink, Shoreline dissipation of infragravity waves, *Continental Shelf Research,* http://dx.doi.org/10.1016/j.csr.2013.11.013

# Shoreline dissipation of infragravity waves

A. T. M. de Bakker*, M. F. S. Tissier, B. G. Ruessink

*Department of Physical Geography, Faculty of Geosciences, Utrecht University, P.O. Box 80115, 3508 TC Utrecht, The Netherlands*

**Abstract**

Infragravity waves (0.005 - 0.05 Hz) have recently been observed to dissipate a large part of their energy in the short-wave (0.05 - 1 Hz) surf zone, however, the underlying mechanism is not well understood. Here, we analyse two new field data sets of near-bed pressure and velocity at up to 13 cross-shore locations in $\lesssim$ 2.5 m depth on a $\approx$ 1:80 and a $\approx$ 1:30 sloping beach to quantify infragravity-wave dissipation close to the shoreline and to identify the underlying dissipation mechanism. A frequency-domain Complex Eigenfunction analysis demonstrated that infragravity-wave dissipation was frequency dependent. Infragravity waves with a frequency larger than $\approx$ 0.0167-0.0245 Hz were predominantly onshore progressive, indicative of strong dissipation of the incoming infragravity waves. Instead, waves with a lower frequency showed the classic picture of cross-shore standing waves with minimal dissipation. Bulk infragravity reflection coefficients at the shallowest position (water depth $\approx$ 0.7 m) were well below 1 ($\approx$ 0.20), implying that consider-

*Corresponding author. Tel.: +31 30 253 7453; fax: +31 30 253 1145.
*Email address:* `a.t.m.debakker@uu.nl` (A. T. M. de Bakker)

able dissipation took place close to the shoreline. We hypothesise that for our data sets infragravity-wave breaking is the dominant dissipation mechanism close to the shoreline, because the reflection coefficient depends on a normalised bed slope, with the higher infragravity frequencies in the mild-sloping regime where breaking is known to dominate dissipation. Additional numerical modelling indicates that, close to the shoreline of a 1:80 beach, bottom friction contributes to infragravity-wave dissipation to a limited extent, but that non-linear transfer of infragravity energy back to sea-swell frequencies is unimportant.

*Key words:*

Infragravity waves, energy flux, reflection, dissipation, wave breaking

---

## 1. Introduction

Infragravity waves are 20-200 s motions in the ocean surface that are strongest near the shore, and may be responsible for beach (e.g. Russell, 1993) and dune (Van Thiel de Vries et al., 2007) erosion. Infragravity waves can arise from the non-linear energy transfer from $<$ 20 s sea and swell waves. In deep water the transfer of energy is non-resonant and the height of infragravity waves is a few millimeters at most. In coastal and nearshore water depths the energy transfer becomes near-resonant and, as a consequence, infragravity-wave height can increase rapidly to over 1 m (e.g. Guza and Thornton, 1982; Ruessink et al., 1998; Sénéchal et al., 2011). During the breaking of the sea and swell waves, the infragravity waves propagate towards the beach as free waves and reflect from the shoreline. The simultaneous presence of shoreward propagating and reflected infragravity waves gives rise to a standing wave pattern (Guza and Thornton, 1985).

The predominantly observed cross-shore standing nature implies that infragravity-wave dissipation in the sea-swell surf zone must generally be small. Interestingly, Guza and Thornton (1985) observed infragravity frequencies above 0.03 Hz to show an increasingly progressive wave pattern, suggesting some infragravity-wave dissipation. The (crudely estimated) infragravity-wave reflection coefficient, the ratio of seaward to shoreward propagating infragravity-wave energy flux, of 0.5 confirms this. Other observations indicate (bulk, i.e. frequency integrated) infragravity-wave dissipation to be considerably higher. For example, Ruessink (1998b) observed the infragravity wave-height to decrease rather than to increase onshore in the surf zone of a low-sloping ($\approx 1:200$) multiple barred system. For the same site, Ruessink et al. (1998) found swash spectra to saturate well into the infragravity band, indicative of energy dissipation due to infragravity-wave breaking. Later, saturation at infragravity frequencies was also observed at other sites (Ruggiero et al., 2004; Sénéchal et al., 2011; Guedes et al., 2013).

Since these initial observations, several infragravity-wave dissipation mechanisms have been suggested in the literature. Henderson and Bowen (2002) mentioned bottom friction as the dominant mechanism; however, the implied drag coefficient in the bottom friction formulation is unrealistically high for sandy beaches (Henderson et al., 2006). For coral reefs, bottom friction does play a dominant role in the energy dissipation of infragravity waves, as the friction coefficient is an order of magnitude larger, $c_f \approx$ 0.02-0.05, than on sandy beaches where $c_f \approx 0.005$ is already quite high (Pomeroy et al., 2012; Van Dongeren et al., 2013). Instead, Henderson et al. (2006) suggested the existence of non-linear energy transfer back to sea-swell frequencies through triad interactions, as did Thomson et al. (2006) and Guedes et al. (2013). Thomson et al. (2006) show this non-linear transfer to be particularly relevant in the inner surf zone in water depths larger than about 1 m, where sea-swell energy still dominates over infragravity energy. Closer to the shore, their incoming and outgoing infragravity fluxes were about equal, suggesting minimal infragravity-wave dissipation at the shoreline. Instead, Battjes et al. (2004) and Van Dongeren et al. (2007) observed dissipation to be strongest at a laboratory shoreline and suggested that infragravity-wave breaking played a role. The concept of infragravity-wave breaking is supported by Lin and Hwung (2012), who performed high-resolution laboratory experiments over varying (1:10 to 1:60) sloping beds. Furthermore, Nazaka and Hino (1991) observed infragravity waves on a laboratory reef to possess a bore-like shape, similar to breaking sea-swell waves.

Based on the work of Battjes (1974), Van Dongeren et al. (2007) found that the shoreline amplitude reflection coefficient $R$ of monochromatic infragravity waves is related to a normalized bed slope, $\beta_H$, as $R = 2\pi{\beta_H}^2$, with

$$\beta_H = \frac{\beta\ T}{2\pi}\sqrt{\frac{g}{H^+}}. \tag{1}$$

Here, $\beta$ is the bed slope, $H^+$ is the height of the incoming infragravity wave with period $T$, and $g = 9.81$ m/s$^2$ is the gravitational acceleration. This parameter is based on the concept that a given bed slope appears steeper to longer (lower frequency) waves than it does to shorter (higher frequency) waves. On a steeper slope, more energy will be reflected (i.e., less energy will be dissipated). Van Dongeren et al. (2007) delineated a mild-sloping regime ($\beta_H < 1.25$) where energy is dissipated by infragravity-wave breaking, from a steep-sloping regime ($\beta_H > 1.25$) where $R \approx 1$ and almost no infragravity-wave energy dissipates. The transition at approximately $\beta_H = 1.25$ is similar to the value previously found for the onset of short wave breaking (Battjes, 1974). Additionally, Van Dongeren et al. (2007) showed that in the infragravity breaking-zone the dominant triad interactions are infragravity self-self interactions, rather than the infragravity sea-swell interactions investigated by Henderson et al. (2006), Thomson et al. (2006) and Guedes et al. (2013). Recently, Ruju et al. (2012) suggested, based on a numerical evaluation of the radiation stresses and the infragravity-wave energy balance, that both breaking and non-linear energy transfer could play a role, each mechanism in another water depth range within the short-wave surf zone. Seaward of the inner short-wave surf zone where short waves still dominate over infragravity waves, the infragravity waves transferred their energy back to the short waves through triad interactions, while in the inner surf zone the remaining infragravity energy was most likely dissipated due to infragravity-wave breaking. Despite the extensive modelling work, laboratory- and field experiments that have been devoted to identifying the possible sources of infragravity energy loss, the exact infragravity-dissipation mechanism(s) is(are) still unclear and most process-based models do not account for the significant infragravity-wave dissipation observed in the field.

Here, we present field observations of infragravity waves from two field sites contrasting in beach slope with the specific focus on the shoreline dissipation source. In this way, we extend the primarily laboratory (Van Dongeren et al., 2007) and modelling based work (Ruju et al., 2012) on infragravity-wave breaking. In Section 2 we describe the data sets, and introduce our analysis methods. The results and the likely relevance of infragravity-wave breaking to inshore dissipation are described in Section 3. In Section 4, we examine the role of both bottom friction and non-linear energy transfer in infragravity dissipation using numerical modelling. Furthermore, we here elaborate the effect of beach slope on infragravity-wave reflection. Our main results are summarized in Section 5.



## 2. Methods

### *2.1. Field site and instruments*

Field observations of near-bed pressure and velocity were collected during two field campaigns in the Netherlands. The first campaign was carried out during autumn 2010, on the low-sloping North Sea facing Ballum beach ($\approx 1:80$) on the barrier island Ameland (Ruessink et al., 2012). The second field campaign took place during autumn 2011 on the steeper-sloping Egmond beach ($\approx 1:20-1:40$). During both field experiments, instruments were placed in a cross-shore array in the intertidal zone. The arrays extended from the low-tide spring level (1 m below Mean Sea Level, MSL) to the high-tide level that is expected for a typical autumn storm coinciding with spring tide (1.5 m above MSL), see Figure 1. Along each transect 9 pressure transducers (PTs) were placed that sampled continuously at 5 Hz. At three locations, in between these PTs, electromagnetic flowmeters (EMFs) and other PTs were co-located, sampling continuously at 4 Hz. Additionally, the Ameland array comprised a rig equipped with a PT (sampling frequency of 4 Hz) and three Sontek Acoustic Doppler Velocimeter Ocean (ADVO) probes (sampling frequency of 10 Hz). The ADVO probes were placed in a vertical array (PT5 at Ameland) to study surf zone turbulence (Grasso and Ruessink, 2012) (Figure 1). During both deployments, the array thus comprised 12 (Egmond) or 13 (Ameland) instrumented positions, all with PTs and three (Egmond) or four (Ameland) positions with equipment to measure flow velocities. The PTs were positioned at around 5 to 10 cm above the bed; the EMFs were repositioned every day to a height of about 20 cm above the bed. The transect was measured several times with a Differential Global Positioning System (DGPS) during the Ameland campaign, and daily at Egmond because of the higher morphological variability (see Figure 1). The bed material had a median grain size of about 200 $\mu$m and 300 $\mu$m on Ameland and Egmond, respectively.

### 2.2. Initial data processing

At both sites, data were collected for approximately six weeks. For each tide, a block of 2 hours of data centred around high tide was selected. During these two hours, wave statistics (height, period) and the water level were approximately stationary. The data were corrected for small (< 1 s/day) clock drifts. The pressure data were converted to free surface elevation, with a depth correction using linear wave theory. When part of the data at a specific location showed intermittently dry and wet conditions, the entire series was removed. Thus, all data analysed here were collected seaward of the swash zone. As we focus on cross-shore infragravity dynamics, two selection methods were defined regarding alongshore low-frequency (0.005 - 0.05 Hz) dynamics. Firstly, high tides with shear-wave variance exceeding 50% of infragravity-wave variance (Lippmann et al., 1999) at any location with velocity data, were removed from the data set. Secondly, tides with alongshore-velocity variance in the infragravity band exceeding 50% of the cross-shore infragravity velocity variance, were also removed from the data set. In total, 57 2-hour blocks were retained in the Ameland data set and 15 in the Egmond data set.

The retained pressure and velocity data were quadratically detrended, when needed resampled to 4 Hz, and filtered into high sea-swell (0.05-1 Hz) and infragravity (0.005-0.05 Hz) frequencies. The significant wave height for both sea-swell ($H_{ss}$) and infragravity ($H_{inf}$) waves was calculated as four times the standard deviation of the sea surface elevation of each frequency range. For the calculation of incoming and outgoing frequency-dependent energy fluxes ($F^+(f)$ and $F^-(f)$, where $f$ is frequency), two complimentary methods were used (see Appendix A). The first is a local method (Sheremet et al., 2002, Eqs. A1-A2) requiring pressure and cross-shore velocity; it can therefore be applied here at a limited number of positions only. The second method is the array method of Van Dongeren et al. (2007). It requires pressure observations only and can therefore provide flux estimates at more locations than the local method; however, the results are somewhat sensitive to array size. Both methods are compared in Appendix A. By integrating over the infragravity frequency range, bulk infragravity fluxes were computed, Eq. (A3). The ratio of $F^-(f)$ to $F^+(f)$ is the reflection coefficient $R^2(f)$. Analogously, we also estimated a bulk infragravity reflection coefficient, Eq. (A3).

As pointed out earlier, the beach slope $\beta$, close to shore, is a potentially important variable for the amount of energy dissipation. Therefore, the beach slope of the swash zone was calculated for every high tide. As we have no swash measurements and focus on infragravity-wave dynamics, the infragravity swash height was estimated as (Stockdon et al. (2006), their empirically defined Eq. 12)

$$S_{inf} = 0.06(H_0 L_0)^{1/2}, \tag{2}$$

where $H_0$ is the deep-water significant wave height, and $L_0$ is the deep-water wave length ($L_0 = gT_0^2/2\pi$). The centre of the swash zone was taken as the location where the mean water level at the shallowest sensor (with respect to MSL) intersected with the beach face. This resulted in $\beta$ = 1:27 to 1:80 at Ameland, and $\beta$ = 1:22 to 1:50 at Egmond.

### *2.3. Experimental conditions*

Offshore wave conditions ($H_0$ and $T_0$) were measured during the Ameland campaign by a directional wave buoy positioned in a water depth of about 24 m. The offshore water level fluctuations ($\eta_0$) were measured at the tidal station Terschelling Noordzee, located some 20 km to the west of the instrument array. Offshore wave conditions during the Egmond campaign were measured by a non-directional buoy, located ≈ 20 km to the southwest of the instrument array. The offshore water levels were measured at the tidal stations IJmuiden Buitenhaven and Petten Zuid, located ≈ 15 km south and north of Egmond, respectively. As Egmond is about midway between the two stations, $\eta_0$ at Egmond was computed as the average of $\eta_0$ at IJmuiden and Petten, see also Van Enckevort and Ruessink (2001).

At Ameland, the $H_0$ during the 57 selected high tides ranged from 0.4 to 4.4 m, and $T_0$ from 3.1 to 7.0 s. At Egmond, the 15 $H_0$ values varied from 0.3 to 3.6 m, and $T_0$ from 4.1 s to 8.0 s. The $\eta_0$ for all retained tides were typically between -0.5 and 0.6 m at Ameland, and between -0.9 and 0.6 m at Egmond. The $H_{inf}$ at the most seaward positioned sensor ranged between 0.2 and 0.5 m at Ameland, and between 0.03 and 0.4 m at Egmond. Infragravity waves became increasingly important in shallower water and even dominated the water motion at the most shoreward sensors on Ameland during the most energetic conditions (Table 1). At both field sites $H_{inf}$ correlated well with $H_0$, Fig. 2, although some saturation in $H_{inf}$ for $H_s > 3$ m may be seen at Ameland (Fig. 2). The best-fit linear line had a skill $r^2$ of around 0.95 for both data sets (Table 1). The constant of proportionality $m$ at all locations for both data sets was $\approx 0.11$ (Table 1), and contrary to expectations (e.g. Holman, 1983) did not increase notably towards the shore.

While $H_{inf}$ correlated well with the offshore significant sea-swell wave height $H_0$, $H_{ss}$ did not. Instead, $H_{ss}$ was tide-modulated and positively dependent on $\eta_0$. This suggests that the instruments were within the surf zone. To check whether the instruments were indeed in the surf zone during high tide, the extent of the surf zone was estimated by running the Battjes and Janssen (1978) wave model from $\approx 20$ m depth to the shore. If the local energy flux reached 85% of its offshore value, the edge of the surf zone was assumed to be reached. During the Ameland campaign, the transect was completely located within the surf zone during 58% of the 57 high tides. For Egmond, this was the case for 45% of the 15 high tides. During less energetic wave conditions, the most seaward positioned sensors were located outside the surf zone, but the most onshore positioned sensors were always located in the surf zone. Consistent with predictions, $H_{ss}$ decreased onshore from P1 to the shallowest sensor. The ratio of $H_s$ to water depth $h$ at the shallowest sensor had a measured campaign-averaged value of 0.64 at Ameland, and

0.66 at Egmond. This is well above a typical value of $\approx 0.3$ that marks the outer edge of a low-sloping surf zone (Ruessink, 1998a). The high average values indicate that the shallowest sensors were always located in the inner surf zone, just seaward of the swash zone.

## 3. Results

Figure 3 shows the incoming and outgoing bulk infragravity fluxes, $F^+$ and $F^-$, for a representative low-, intermediate- and high-energy tide at Ameland (Figs. 3 a, b and c) and Egmond (Figs. 3 e, f and g). As can be seen, $F^+$ exceeds $F^-$ at all locations at both sites, and especially at Ameland. $F^+$ decreases over the transect in the onshore direction at some high tides (e.g., Fig. 3b) (discussed further in Section 4). However, a roughly equally large part of the $F^+$-reduction takes place shoreward of the most inshore located sensor, thus over a rather short cross-shore stretch near the shoreline. To demonstrate the infragravity dissipation at the shoreline more extensively, Figure 4 displays the bulk $R^2$ for the most shoreward located sensor with both pressure and velocity sensors (PT10 at Ameland and PT8 at Egmond) versus the Iribarren number $\xi_0$ (Battjes, 1974),

$$\xi_0 = \frac{\tan\beta}{(H_0/L_0)^{1/2}}. \tag{3}$$

The difference in beach slope between the two field sites is visible by the slightly higher $R^2$ (0.4-0.7) at Egmond than at Ameland (0.3-0.6), and the different $\xi$ range for both sites. On the whole, the $R^2 < 1$ imply that infragravity waves must have dissipated considerable energy shoreward of the innermost sensor during all tides at both sites.

To explore the frequency-dependent cross-shore infragravity pattern, we performed a frequency-domain Complex Empirical Orthogonal Function (EOF) of the pressure fluctuations in the [0.005 - 0.05 Hz] frequency band as outlined in Henderson et al. (2000). The method computes the dominant cross-shore structure of infragravity waves by performing an eigenfunction analyses of the cross-spectral matrix at each infragravity wave frequency. The results for 3 infragravity frequencies of the 3 Ameland tides of Figure 3 are shown in Figure 5. The non-dimensional spatial amplitude $A$ (first mode) of the lowest selected frequency $f = 0.011$ Hz ($T = 90$ s) shows a well-developed (anti)nodal structure, with antinodes at $x \approx 50$ m and $x \approx 150$ m and a node at $x \approx 125$ m (Fig. 5a). At the node, the phase ($\phi$) jumps $\pm 180^\circ$ (Fig. 5d). This is the classical picture of a standing wave with minimal energy dissipation. The limited energy loss is visible as well by the high $R^2$ (0.4 - 1), Figure 5g. For higher infragravity-wave frequencies, the pattern is markedly different (Fig. 5b). At $f = 0.022$ Hz ($T = 45$ s) the (anti)nodal structure is still apparent, however the phase difference now shows an approximately linear increase in the shoreward direction. This reflects a combination of a standing and a progressive wave pattern. The associated $R^2$ have decreased considerably to $R^2 = 0.1$ - 0.6. For even higher frequencies, for example at $f = 0.044$ Hz ($T = 22.5$ s), the pattern is predominantly progressive, and inshore dissipation must therefore be significant. The (anti)nodal variations have changed into a monotonic decreasing trend for tides 5 and 41, and the corresponding $R^2$ are less than 0.2, even at the shallowest position. On the contrary, for the low-energy tide 23 the non-dimensional amplitude increases onshore, suggesting that infragravity-wave energy must have dissipated only shoreward of the shallowest sensor (Fig. 5c); the increase most likely reflects the ongoing energy transfer from short to infragravity waves seaward of the surf zone (e.g. Janssen et al., 2003; Battjes et al., 2004). Figure 5 thus illustrates that the shoreline infragravity-wave dissipation is frequency-dependent.

When considering the 57 selected Ameland tides, the change from cross-shore standing to predominantly onshore progressive infragravity waves is typically around $f = 0.0167$ Hz ($T = 60$ s). This implies that frequencies $>$ 0.0167 Hz dissipate energy before reaching the shoreline. For the Egmond data, the cross-shore infragravity wave pattern displays a similar dependence with frequency; however, the transition from standing to progressive waves is approximately at $f = 0.0245$ Hz ($T = 40$ s). This difference in transition is probably due to the larger $\beta$ at Egmond. Especially at the start of the Egmond campaign, $\beta$ was particularly large ($\approx$ 1:25), and almost all infragravity frequencies displayed a predominantly standing pattern. This is further discussed in Section 4.1.

Averaged over all selected tides, bulk $R^2$ ($\pm$ one standard deviation) determined for the [0.0167-0.05] Hz band for Ameland, and the [0.0245-0.05]

Hz band for Egmond were 0.23 ± 0.11, and 0.18 ± 0.13 respectively, at the centre position in the most landward PT array in the Van Dongeren et al. (2007) method. This corresponds to PT5 to PT12 for Ameland and PT8 to PT11 for Egmond, depending primarily on $\eta_0$. For the [0.005-0.0167] Hz (Ameland) and the [0.005-0.0245] Hz (Egmond) bands, bulk $R^2$ amounted to 0.60 ± 0.11, and 0.65 ± 0.25, respectively. The bulk $R^2$ for the highest frequencies indicate dissipation shoreward of the shallowest location, in $h$ less than on average $\approx$ 0.65 m for Ameland, and $h \approx$ 0.75 m for Egmond. In other words, the dissipation is localized near the shoreline and is limited to a short cross-shore stretch. The distance between the shallowest position and the shoreline is typically some 55 m for Ameland and 25 m for Egmond, which is much smaller than the local infragravity wave length in the [0.0167-0.05 Hz] and [0.0245-0.05 Hz] band. This practically rules out bottom friction as the dominant infragravity-wave dissipation mechanism.



To investigate the possible role of infragravity-wave breaking, Figure 6 shows $R$ for selected frequency bands versus $\beta_H$. Here, $H^+$ was estimated as $H^+ = 4\sqrt{\int_{f-\Delta f}^{f+\Delta f} E^+(f)df}$, with a frequency resolution $\Delta f$ of 0.00111 Hz. If $\Delta f$ were altered by a factor of two, then $H^+$ would be altered by a factor of approximately $\sqrt{2}$, and $\beta_H$ by approximately 20%. The trend of $R$ with $\beta_H$ would, however, remain unchanged. As can be seen, $R$ is indeed related to $\beta_H$, however, the transition from mild-to-steep sloping regime is more gentle and at higher $\beta_H$ ($\approx$ 3 for Ameland) than for the laboratory data set of Van Dongeren et al. (2007) where the transition was at $\beta_H \approx$ 1.25. This is probably because Van Dongeren et al. (2007) estimated $\beta_H$ and $R$ for the seaward edge of the short-wave swash zone, whereas our estimates are for a slightly more seaward location. The lack of accurate swash observations along with the used infragravity flux separation method limits us to a more seaward position than our most landward positioned instrument. An additional point is that the choice of $H^+$ and $T$ in a random wave field is less straightforward compared to the monochromatic infragravity-wave cases in Van Dongeren et al. (2007).

On the whole, Figure 6 lends support that in our Ameland data set frequencies above 0.0167 Hz are in the mild-sloping regime ($\beta_H < 3$) and loose energy due to breaking, while frequencies lower than 0.0167 Hz are in the steep sloping regime ($\beta_H > 3$), and reflect almost completely. For Egmond the transition is less distinct, but higher frequencies ($f > 0.0245$ Hz) have relatively low $R$ and can be assigned to the mild-sloping regime, whereas lower frequencies ($f < 0.0245$ Hz) have relatively high $R$ and can be assigned to the steep sloping regime.

## 4. Discussion

Our results show that infragravity waves dissipate a considerable part of their energy over a short cross-shore stretch close to the shoreline. The dissipation is frequency dependent, consistent with earlier findings of field (Henderson et al., 2000; Guedes et al., 2013) and laboratory studies (Battjes et al., 2004; Van Dongeren et al., 2007). Our results differ from those of Thomson et al. (2006), as they observed the largest dissipation in water depths ($h > 0.65$ m) in the inner short-wave surf zone, and measured $R^2 \approx 1$ just seaward of the swash. Because in our case a large part of the dissipation took place in very shallow water ($h \lesssim 0.65$-$0.75$ m) and over a short cross-shore distance (25-55 m), we hypothesised breaking to be the dominant dissipation mechanism. This was supported by the observed dependence of $R$ on $\beta_H$ (Fig. 6), although, in detail, there are some differences with Van Dongeren et al. (2007) laboratory findings.

In this section we investigate the observed differences between the Egmond and Ameland data set in more detail by performing a number of numerical simulations with the SWASH model (version 1.20). In addition, the SWASH model is used to study the influence of both bottom friction and non-linear energy transfer on the infragravity-wave energy dissipation. The governing equations of the SWASH model are the non-linear shallow water equations and account for non-hydrostatic pressure. Our primary motivation to use the model is the capability of SWASH to simulate long and short wave transformation from the shoaling to swash zone (Zijlema et al., 2011; Smit et al., 2013). Second-order bound infragravity waves are added at the offshore boundary so that the wave field is consistent with the non-linear momentum equations. For a more in-depth description of the model, see Zijlema et al. (2011), Rijnsdorp et al. (2012) and Smit et al. (2013). We ran the model in profile (one-dimensional, 1D) mode for 3 monotonic sloping beaches ($\beta$ = 1:80, 1:40 and 1:20), starting in 20-m water depth. We used the default settings, with two horizontal layers. The temporal and cross-shore spatial resolutions are 0.005 s and 0.25 m, respectively. Jonswap spectra for 3 wave conditions were used as input (1) $H_0 = 1$ m, $T_0 = 5.25$ s, (2) $H_0 = 2$ m, $T_0 = 6.5$ s, (3) $H_0 = 3$ m, $T_0 = 8$ s, loosely based on the Ameland data set. All conditions were initially run without bottom friction (drag coefficient $c_f = 0$). We realise that by running the model in profile mode we ignore the effect of directional spreading on infragravity wave generation (Herbers et al., 1999; Guza and Feddersen, 2012) and are likely to overestimate $H_{inf}$. Therefore, we forego a detailed data-model comparison and consider our modelling as exploratory. From each run, we extracted the instantaneous sea surface elevation (output frequency of 4 Hz) and orbital motion, allowing to estimate $H_{ss}$ and $H_{inf}$ as well as $F^{\pm}$ with the Sheremet et al. (2002) approach. Indeed, the model overpredicts $H_{inf}$; for example with $H_0 = 3$ m on the 1:80 slope, $H_{inf} \approx 0.7$ m close to the shore, about twice as high as in the observations (Fig. 2a).

### *4.1. Slope effects*

To elaborate the observed difference in transition frequency from standing to progressive waves between Ameland and Egmond, simulations were made for one 1D profile with a monotonic 1:80 sloping beach, and two additional profiles with a steeper foreshore slope. At $h = 2$ m, which is shoreward of the short-wave breakpoint, the slope of 1:80 was changed into 1:40 or 1:20, see Figure 7b. This location for the slope change was chosen so that the incoming infragravity-wave fluxes were the same until the point of short-wave breaking, allowing to compare the processes close to shore. Figure 8a shows that for $H_0$ = 2 m, the incoming infragravity-wave fluxes indeed increase equally to the point of short-wave breaking and then all decrease; slightly more shoreward, on the 1:20 and 1:40 slopes, the fluxes increase again, indicating diminished infragravity-wave dissipation (with respect to the 1:80 results) and even infragravity wave shoaling. The outgoing fluxes differ greatly depending on the slope. For the 1:80 slope, barely any infragravity-energy is predicted to reflect from the shore, while for the 1:20 slope the reflection obviously must have been higher. When examining the frequency dependence, the results for the 1:20 slope show high $R^2$ for the entire infragravity wave band, whereas for the 1:40 (1:80) slope only frequencies $< 0.025$ Hz ($< 0.01$ Hz) show high $R^2$.

The dependence of $R$ on $\beta_H$ as observed in the field (Fig. 6) is reproduced for the SWASH simulations (Fig. 8). For the steep 1:20 foreshore slope (Fig. 8a), $R$ is $\approx 1$ for all frequencies, while for the 1:80 foreshore slope, $R$ drops off rapidly with increasing frequency to near-zero reflection. Intriguingly, the model results do not follow the $R = 2\pi\beta_H^2$ dependence and, as in the field data, the transition to $R \approx 1$ is at $\beta_H \approx 3$ (Figs. 8a-b). Overall, this confirms our findings of an overall larger reflection, and a frequency transition at higher frequencies at Egmond than at Ameland, due to the steeper beach slope at the former location.

### *4.2. Bottom friction*

Although the field and model data show a tendency of infragravity-wave energy dissipation due to infragravity wave breaking (Figs. 6 and 8), one may also expect bottom friction to be important in shallow water on low-sloping beaches. Therefore additional simulations were run for the low-sloping 1:80 bed profile that resembles the Ameland field site. The 3 wave-conditions were re-run, now including bottom friction, using a relatively high (Feddersen et al., 1998) drag coefficient $c_f$ of 0.005.

Figure 9 shows the predicted cross-shore evolution of $H_{ss}$ and $H_{inf}$ for the 3 conditions with and without bed friction for the 1:80 slope. As can be seen, even without bottom friction, $H_{inf}$ stops to increase when the short waves start to break. The shoreward bulk infragravity-wave energy fluxes additionally decrease from this point onward (not shown), however the largest energy dissipation takes place close to the shore, consistent with our field data. With $c_f = 0.005$, the cross-shore evolution of $H_{inf}$ does not alter considerably.

To compare the model results with the field measurements, $R^2$ values were determined for a water depth of about 0.65 - 0.7 m. Overall, $R^2$ was about 0.15 for the cases with no friction, and 0.08 for the cases with friction. This is slightly lower than the measured values, probably because the overestimated $H_{inf}$ caused more pronounced dissipation. The frequency dependence seen in the field data is also produced by the model for both $c_f = 0$ and $c_f = 0.005$. The model showed negligible $R^2$ at frequencies higher than $\approx 0.01 - 0.02$ Hz for $H_0 = 1$ m; with larger $H_0$ this threshold shifts to lower frequencies. On the whole, our modelling indicates that bottom friction is at best a secondary effect for infragravity-wave dissipation at the shoreline.

### *4.3. Non-linear energy transfer*

A third mechanism that could explain the infragravity-wave energy dissipation is the non-linear energy transfer back to sea-swell frequencies (Henderson et al., 2006; Thomson et al., 2006; Ruju et al., 2012; Guedes et al., 2013). To examine this possibility, bispectral analysis was performed on the SWASH model results. For an in-depth description of bispectral analysis we refer to Hasselman et al. (1963), Elgar and Guza (1985) and Collis et al. (1998). Following Herbers et al. (2000), we focus on the imaginary part of the bispectra, which indicates the direction and magnitude of the non-linear energy transfer. Negative (positive) values are indicative of a loss (gain) of energy by triad interactions. The normalized magnitude of the bispectrum, called bicoherence, shows the relative strength of the coupling of triads. As our infragravity-energy dissipation is strongest in our Ameland data set, we here focus on the $\beta$ = 1:80 simulations without bed friction. The incoming wave signal for all 3 wave conditions, determined at each location with the Guza et al. (1984) approach, was processed by dividing the timeseries into blocks of 15 min (total signal length per simulation was about 2 hours). Subsequent averaging of the bispectral estimates over 7 frequencies resulted in a frequency resolution of 0.0078 Hz, 210 degrees of freedom and a 95%

confidence level for non-bicoherence of 0.169 (Haubrich, 1965).

Figure 10 displays the bispectral results for three locations on the 1:80 slope for $H_0 = 2$ m. Offshore of the short-wave surf zone (Fig. 10d), infragravity-wave frequencies receive energy through difference interactions between the short waves. The corresponding biphases (not shown) are close to $\pi$, consistent with the forcing of a bound infragravity wave. In the centre of the short-wave surf zone the coupling between sea-swell frequencies and infragravity frequencies stays strong (Fig. 10e), overall, the infragravity frequencies still receive energy from the short waves. A positive infragravity-infragravity interaction at about (0.015,0.015) Hz is present now too. Close to the shore, where the infragravity waves dominate the power spectrum, statistically significant bispectral estimates are within the infragravity frequency range only. Interestingly, the higher infragravity frequencies are transferring energy to the lower infragravity frequencies. Overall, the bispectral analysis shows that non-linear energy transfers from infragravity frequencies to sea-swell frequencies do not seem to play a role close to the shore. For $H_0 = 1$ m and $H_0 = 3$ m, the bispectra evolve in about the same way. In more detail, the bicoherence is stronger overall (up to 0.9) in the $H_0 = 3$ m simulation, and all infragravity frequencies loose energy close to shore. In the $H_0 = 1$ m simulation, the bicoherence values are, in contrast, lower and close to shore energy transfers within the infragravity-frequency range are rather weak.

Although our data and model analyses indicate that shoreline breaking is the dominant mechanism for infragravity-wave dissipation close to the shoreline (confirming the laboratory study of Van Dongeren et al. (2007)), we cannot rule out that other mechanisms may be relevant in $h > 0.75$ m and may be responsible for the decline in $F^+$ seen over parts of the transect (e.g. Fig. 3b), especially during high-energy conditions. It may be that infragravity-wave breaking is extending further seaward. This, and a more in-depth analysis on the role of non-linear energy transfer within the infragravity range, awaits further study.

## 5. Conclusions

Observations of near-bed pressure and velocity collected in cross-shore arrays spanning the intertidal zone of two beaches show that infragravity energy dissipation can be considerable and is frequency dependent. Waves with frequencies $> 0.0167$ Hz at Ameland and $> 0.0245$ Hz at Egmond are shoreward progressive and dissipate almost completely ($R^2 \approx 0.23 \pm 0.11$ and $\approx 0.18 \pm 0.13$). Waves with lower frequencies possess a cross-shore standing wave pattern and conserve a large part of their energy ($R^2 \approx 0.60 \pm 0.11$ at Ameland, and $0.65 \pm 0.25$ at Egmond). As a large part of the infragravity-wave dissipation takes place in very shallow water ($h < 0.65-0.75$ m), and is thus limited to a short cross-shore stretch close to the shoreline, infragravity-wave breaking seems likely to be the dominant infragravity-wave dissipation mechanism. This is confirmed by the dependence of $R$ on the normalised bed slope $\beta_H$, which shows that for frequencies $> 0.0167$ Hz at Ameland, and frequencies $> 0.0245$ Hz at Egmond, the infragravity waves are in the mild sloping regime, where breaking dominates dissipation. Exploratory modelling shows that the bulk infragravity reflection coefficient and the frequency at which standing waves change into onshore progressive waves increases with foreshore slope. The latter finding is consistent with the differences between the Ameland and Egmond data sets. Additional modelling shows that close to the shoreline, bottom friction is at best a secondary dissipation mechanism and that non-linear energy transfers from infragravity frequencies to sea-swell frequencies are not important to infragravity energy dissipation.

## A. Reflection coefficients

The frequency-dependent reflection coefficient is defined as the ratio of the offshore to onshore propagating infragravity flux, $R^2(f) = F^-(f)/F^+(f)$. We used two different methods to obtain these energy fluxes. The first method, detailed in Sheremet et al. (2002), can only be applied to locations with collocated pressure and velocity sensors. The energy ($E$) and cross-shore energy fluxes ($F$) are calculated as

$$E^{\pm}(f) = \frac{1}{4}\left[Co_{pp}(f) + \frac{h}{g}Co_{uu}(f) \pm \left(2\sqrt{\frac{h}{g}}\right)Co_{pu}(f)\right], \tag{A.1}$$

$$F^{\pm}(f) = E^{\pm}(f)\sqrt{gh}, \tag{A.2}$$

where $Co_{pu}$ is the $p - u$ cospectrum and $Co_{pp}$ and $Co_{uu}$ are $p$ and $u$ autospectra, respectively ($p$ is pressure, $u$ is cross-shore velocity). Here, auto- and cospectra were calculated by dividing the detrended data into blocks of 15 minutes, using 50% overlap, and tapering each block with a Hamming window of the same length. This resulted in 38 degrees of freedom. Errors in bulk fluxes and $R^2$ owing to the assumption of normal incidence are estimated to be $< 20\%$ (Sheremet et al., 2002).

To estimate $R^2(f)$ for more locations along our transect array (with only PTs), we also applied the array method of Van Dongeren et al. (2007). It is based on the Battjes et al. (2004) approach with modifications for shoaling and phase speed effects. The incoming long waves are assumed to travel with the group velocity $c_g$, whereas the outgoing waves are assumed to propagate with the linear phase speed $\sqrt{gh}$. As in our data water depths are less than $\approx$ 2-3 m, $c_g \sim \sqrt{gh}$. Pressure data from multiple sensors yield $F^{\pm}(f)$ and $R^2(f)$ at the centre of the array. The fluxes were initially calculated using the entire time series as a single block, and then frequency bands were merged to yield the same spectral resolution as in the single-point method.

For both methods, energy fluxes can be integrated over the $[f_{min} \quad f_{max}]$ frequency range to estimate bulk fluxes $F^{\pm}$ and $R^2$:

$$F^{\pm} = \int_{f_{min}}^{f_{max}} F^{\pm}(f)df, \qquad R^2 = F^-/F^+. \tag{A.3}$$

The bulk $R^2$ estimated with the multi-sensor method, using 3 adjacent sensors correlate well (skill $r^2 = 0.69$ and root-mean-square error $\epsilon_{rms} = 0.07$) with those of the single-point method for the $f$ = 0.0167 - 0.05 Hz range, see Figure A.1a; however, for the $f$ = 0.005-0.0167 Hz range the $R^2$ deviate considerably with $r^2 = 0.09$ and $\epsilon_{rms} = 0.31$. By using 5 sensors the $R^2$ agree better, with $r^2 = 0.06$ and $\epsilon_{rms} = 0.11$ (Figure A.1b), although most array $R^2$ are lower than the single point $R^2$. In the paper we used 3 sensors for $f \geq 0.0167$ Hz, and 5 sensors for $f \leq 0.0167$ Hz. For bulk $R^2$ of the entire infragravity wave band we used 3 sensors ($r^2 = 0.55$ and $\epsilon_{rms} = 0.07$), as it compared slightly better to the single-point $R^2$ than with 5 sensors ($r^2 = 0.37$

and $\epsilon_{rms} = 0.07$), compare Figures A.1c-d.

**Acknowledgements**

We are greatly indebted to Marcel van Maarseveen, Henk Markies, Aline Pieterse, Emily McCullough, Joost Brinkkemper, Stefan Verschure and Marijn Boll for their assistance in the field. Ap van Dongeren sent us the infragravity-separation code, and provided useful feedback. We thank Tom Herbers, who helped us greatly with the bispectral code. Pieter Smit provided much appreciated insights in the SWASH model, and gave helpful feedback on the manuscript. We thank the two anonymous reviewers for their insightful comments. Funded by the Netherlands Organisation for Scientific Research (NWO) under contract 821.01.012.

**References**

Battjes, J.A., 1974. Surf similarity, in: Proceedings of the 14th International Conference on Coastal Engineering, ASCE, 466-480.

Battjes, J.A., Bakkenes, H.J., Janssen, T.T., van Dongeren, A.R., 2004. Shoaling of subharmonic gravity waves. Journal of Geophysical Research 109. C02009, doi:10.1029/2003JC001863.

Battjes, J.A., Janssen, J.P.F.M., 1978. Energy loss and set-up due to breaking of random waves, in: Proceedings of the 16th International Conference on Coastal Engineering, ASCE, 570-587.

Collis, W., White, P., Hammond, J., 1998. Higher-order spectra: the bispectrum and trispectrum. Mechanical Systems and Signal Processing 12(3), 375–394.

Elgar, S., Guza, R.T., 1985. Observations of bispectra of shoaling surface gravity waves. Journal of Fluid Mechanics 161, 425–448.

Feddersen, F., Guza, R.T., Elgar, S., Herbers, T.H.C., 1998. Alongshore momentum balances in the nearshore. Journal of Geophysical Research 103, 15667–15676.

Grasso, F., Ruessink, B.G., 2012. Turbulent viscosity in natural surf zones. Geophysical Research Letters 39, L23603, doi:10.1029/2012GL054135.

Guedes, M., Bryan, K.R., Coco, G., 2013. Observations of wave energy fluxes and swash motions on a low-sloping, dissipative beach. Journal of Geophyiscal Research Accepted for publication.

Guza, R., Feddersen, F., 2012. Effect of wave frequency and directional spread on shoreline runup. Geophysical Research Letters 39, L11607, doi:10.1029/2012GL051959.

Guza, R., Thornton, E., Holman, R., 1984. Swash on steep and shallow beaches, in: Proceedings of the 19th International Conference on Coastal Engineering, ASCE, 708-723.

Guza, R.T., Thornton, E.B., 1982. Swash oscillations on a natural beach. Journal of Geophysical Research 87, 483–491.

Guza, R.T., Thornton, E.B., 1985. Observations of surf beat. Journal of Geophysical Research 87, 483–491.

Hasselman, K., Munk, W., MacDonald, G., 1963. Bispectra of ocean waves. Time Series Analysis , 125–139.

Haubrich, R., 1965. Earth noises, 5 to 500 millicycles per second, 1. Journal of Geophysical Research 70, 1415–1427.

Henderson, S.M., Bowen, A.J., 2002. Observations of surf beat forcing and dissipation. Journal of Geophysical Research 107(C11), 3193, doi:10.1029/2000JC000498 .

Henderson, S.M., Elgar, S., Bowen, A.J., 2000. Observations of surf beat propagation and energetics, in: Proceedings of the 27th International Conference on Coastal Engineering, ASCE, 1412-1421.

Henderson, S.M., Guza, R.T., Elgar, S., Herbers, T.H.C., Bowen, A.J., 2006. Nonlinear generation and loss of infragravity wave energy. Journal of Geophysical Research 111, C12007, doi:10.1029/2006JC003539.

Herbers, T., Elgar, S., Guza, R., 1999. Directional spreading of waves in the nearshore. Journal of Geophysical Research 104, 7683–7693.

Herbers, T., Russnogle, N., Elgar, S., 2000. Spectral energy balance of breaking waves within the surf zone. Journal of Physical Oceanography 30, 2723–2737.

Holman, R.A., 1983. CRC Handbook of coastal processes and erosion. CRC Press, Boca Raton, FL. chapter Edge waves and the configuration of the shoreline. pp. 21–34.

Janssen, T.T., Battjes, J.A., van Dongeren, A.R., 2003. Long waves induced by short-wave groups over a sloping bottom. Journal of Geophysical Research 108, 3252, doi:10.1029/2002JC001515.

Lin, Y.H., Hwung, H.H., 2012. Infra-gravity wave generation by the shoaling wave groups over beaches. China Ocean Engineering 26, 1–18.

Lippmann, T., Herbers, T., Thornton, E., 1999. Gravity and shear wave contributions to nearshore infragravity motions. Journal of Physical Oceanography 29, 231–239.

Nazaka, E., Hino, M., 1991. Bore-like surf beat in a reef zone caused by wave groups of incident short period waves. Fluid Dynamics Research 7, 89–100.

Pomeroy, A., Lowe, R., Symonds, G., Van Dongeren, A., Moore, C., 2012. The dynamics of infragravity wave transformation over a fringing reef. Journal of Geophyiscal Research 117, doi:10.1029/2012JC008310.

Rijnsdorp, D.P., Smit, P., Zijlema, M., 2012. Non-hydrostatic modelling of infragravity waves using swash, in: Proceedings of the 33rd International Conference on Coastal Engineering, ASCE, 1-12.

Ruessink, B.G., 1998a. Bound and free infragravity waves in the nearshore zone under breaking and nonbreaking conditions. Journal of Geophysical Research 103, 12.795–12.805.

Ruessink, B.G., 1998b. The temporal and spatial variability of infragravity energ in a barred nearshore zone. Continental Shelf Research 18, 585–605.

Ruessink, B.G., Boers, M., van Geer, P., de Bakker, A., Pieterse, A., Grasso, F., de Winter, R., 2012. Towards a process-based model to predict dune erosion along the dutch wadden coast. Netherlands Journal of Geosciences 91-3, 357–372.

Ruessink, B.G., Kleinhans, M.G., Van den Beukel, P.G.L., 1998. Observations of swash under highly dissipative conditions. Journal of Geophysical Research 103, 3111–3118.

Ruggiero, P., Holman, R.A., Beach, R.A., 2004. Wave run-up on a high-energy dissipative beach. Journal of Geophysical Research 109, C06025, doi:10.1029/2003JC002160.

Ruju, A., Lara, J., Losada, I., 2012. Radiation stress and low-frequency energy balance within the surf zone: A numerical approach. Coastal Engineering 68, 44–55.

Russell, P., 1993. Mechanisms for beach erosion during storm. Continental Shelf Research 13, 1243–1265.

Sénéchal, N., Coco, G., Bryan, K.R., Holman, R.A., 2011. Wave runup during extreme storm conditions. Journal of Geophysical Research 116, C07032, doi:10.1029/2010JC006819.

Sheremet, A., Guza, R.T., Elgar, S., Herbers, T.H.C., 2002. Observations of nearshore infragravity waves: Seaward and shoreward propagating components. Journal of Geophysical Research 107. C8, doi:10.1029/2001JC000970.

Smit, P., Zijlema, M., Stelling, G., 2013. Depth-induced wave breaking in a non-hydrostatic, near-shore wave model. Coastal Engineering 76, 1–16.

Stockdon, H.F., Holman, R., Howd, P., Sallenger Jr, A.H., 2006. Emperical parameterization of setup, swash and runup. Coastal Engineering 53, 573–588.

Thomson, J., Elgar, S., Raubenheimer, B., Herbers, T.H.C., Guza, R.T., 2006. Tidal modulation of infragravity waves via nonlinear energy losses in the surfzone. Geophysical Research Letters 33. L05601, doi:10.1029/2005GL025514.

Van Dongeren, A., Battjes, J., Janssen, T., van Noorloos, J., Steenhauer, K., Steenbergen, G., Reniers, A., 2007. Shoaling and shoreline dissipation of low-frequency waves. Journal of Geophysical Research 112. C02011, doi:10.1029/2006JC003701.

Van Dongeren, A., Lowe, R., Pomeroy, A., Trang, D., Roelvink, D., Symonds, G., Ranasinghe, R., 2013. Numerical modeling of low-frequency wave dynamics over a fringing coral reef. Coastal Engineering 73, 178–190.

Van Enckevort, I.M.J., Ruessink, B.G., 2001. Effects of hydrodynamics and bathymetry on video estimates of nearshore sandbar position. Journal of Geophysical Research 106, 16969–16979.

Van Thiel de Vries, J.S.M., van Gent, M.R.A., Walstra, D.J.R., Reniers, A.J.H.M., 2007. Analysis of dune erosion processes in large-scale flume experiments. Coastal Engineering 55, 1028–1040.

Zijlema, M., Stelling, G., Smit, P., 2011. Swash: An operational public domain code for simulating wave fields and rapidly varied flows in coastal waters. Coastal Engineering 58, 992–1012.

Table 1: Infragravity-wave statistics. The statistics relate to a linear fit between $H_{inf}$ and $H_0$, where $m$ is the constant of proportionality and $r^2$ is the skill, and to the minimum and maximum value of the ratio of the infragravity to sea-swell variance. PT13 at Ameland yielded too few observations to present meaningful statistics.

| Position | Ameland | | | | Egmond | | | |
|---|---|---|---|---|---|---|---|---|
| | $m$ | $r^2$ | $ratio_{min}$ | $ratio_{max}$ | $m$ | $r^2$ | $ratio_{min}$ | $ratio_{max}$ |
| 1 | 0.12 | 0.92 | 0.007 | 0.117 | 0.10 | 0.97 | 0.013 | 0.076 |
| 2 | 0.13 | 0.97 | 0.008 | 0.140 | 0.11 | 0.97 | 0.015 | 0.085 |
| 3 | 0.11 | 0.94 | 0.008 | 0.173 | 0.11 | 0.96 | 0.022 | 0.147 |
| 4 | 0.11 | 0.93 | 0.010 | 0.202 | 0.10 | 0.97 | 0.020 | 0.192 |
| 5 | 0.12 | 0.93 | 0.012 | 0.251 | 0.10 | 0.97 | 0.021 | 0.229 |
| 6 | 0.12 | 0.94 | 0.014 | 0.320 | 0.10 | 0.99 | 0.022 | 0.249 |
| 7 | 0.12 | 0.89 | 0.018 | 0.584 | 0.10 | 0.97 | 0.019 | 0.329 |
| 8 | 0.12 | 0.95 | 0.017 | 0.908 | 0.10 | 0.97 | 0.023 | 0.358 |
| 9 | 0.12 | 0.95 | 0.018 | 0.743 | 0.11 | 0.96 | 0.029 | 0.527 |
| 10 | 0.13 | 0.94 | 0.020 | 1.841 | 0.12 | 0.96 | 0.041 | 1.132 |
| 11 | 0.14 | 0.92 | 0.039 | 3.752 | 0.13 | 0.88 | 0.163 | 0.788 |
| 12 | 0.14 | 0.49 | 1.012 | 4.127 | 0.12 | 0.97 | 0.265 | 0.687 |
| 13 | - | - | - | - | | | | |

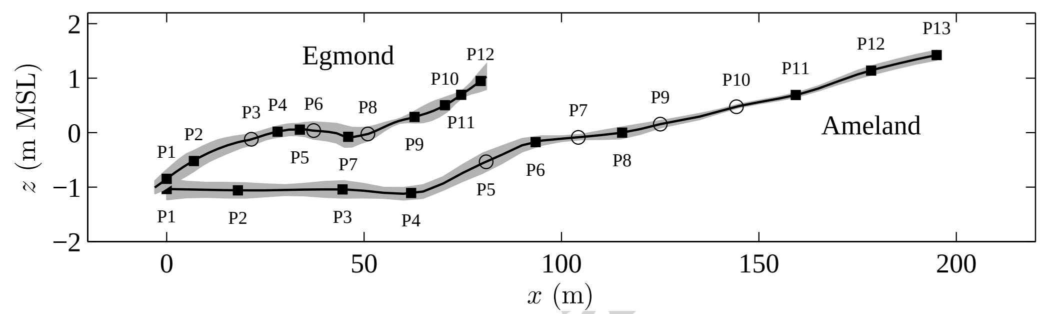


Figure 1: The campaign-mean bed elevation $z$ with respect to MSL versus cross-shore distance $x$ for both Ameland and Egmond. The gray region is the bathymetry standard deviation over time. Black filled squares indicate the PTs, open circles indicate collocated flow meters and PTs.

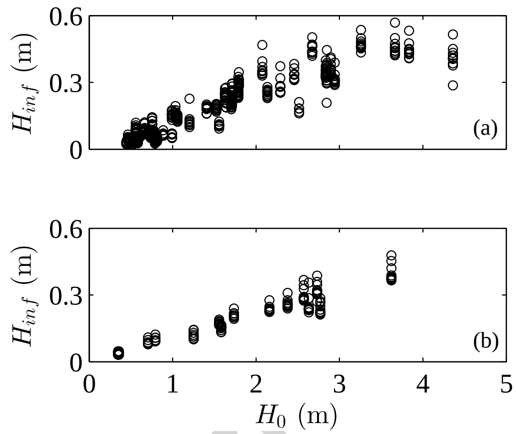


Figure 2: Significant infragravity-wave height ($H_{inf}$) versus offshore significant sea-swell wave height ($H_0$) at (a) Ameland and (b) Egmond. The number of tidal observations per instrument varies from 4 to 57 for Ameland, and from 3 to 15 for Egmond depending on tidal levels and instrument failure.

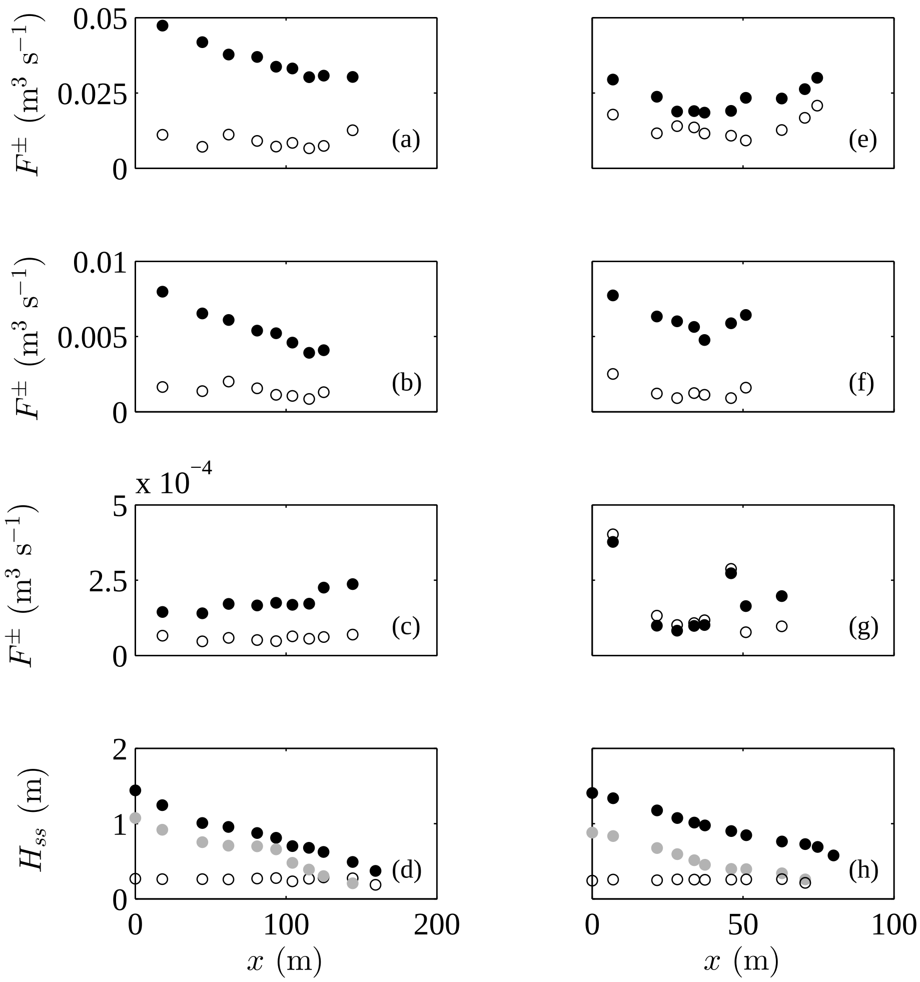


Figure 3: (a-c and e-g) Bulk infragravity energy fluxes $F$ for three selected tides versus cross-shore distance $x$ at (left) Ameland, with a) Tide 5: $H_0 = 2.7$ m, $T_0 = 6.8$ s, b) Tide 41: $H_0 = 1.5$ m, $T_0 = 4.8$ s and c) Tide 23: $H_0 = 0.6$ m, $T_0 = 3.7$ s and (right) Egmond with e) Tide 19: $H_0 = 3.6$ m, $T_0 = 7.0$ s, f) Tide 45: $H_0 = 2.2$ m, $T_0 = 7.4$ s and g) Tide 59: $H_0 = 0.3$ m, $T_0 = 4.8$ s. Dots are the incoming flux $F^+$, circles the outgoing energy flux $F^-$. The bulk infragravity fluxes were calculated with the array-method of Van Dongeren et al. (2007). For reference, (d) and (h) show $H_{ss}$ versus $x$ for each tide, with black/grey/open dots with decreasing $H_{ss}$ and accompanying $F$. Note the scale change from panels a to c (and correspondingly, e to g).

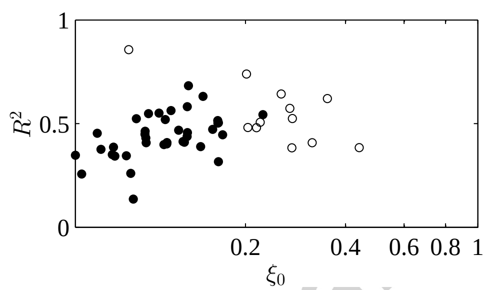


Figure 4: Bulk infragravity reflection coefficients $R^2$ for all retained high tides versus the Iribarren number $\xi_0$. Dots are P10 at Ameland ($h \approx 0.2 - 1.5$ m), and circles are P8 at Egmond ($h \approx 0.3 - 1.8$ m). The bulk infragravity fluxes were calculated with the single-point method of Sheremet et al. (2002).

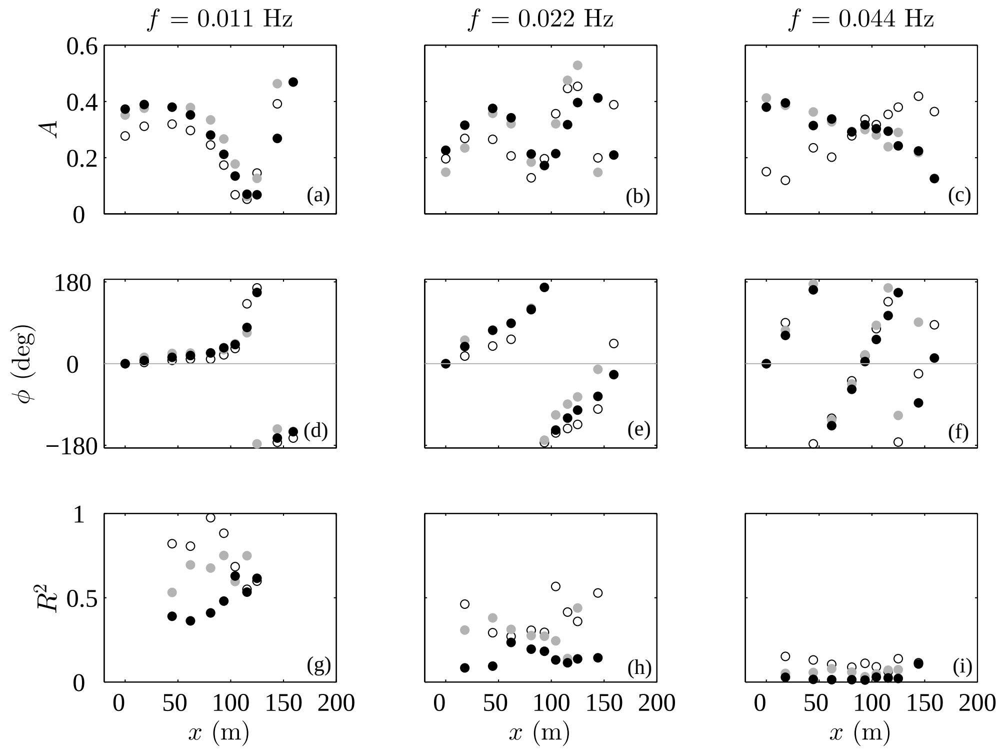


Figure 5: (a-c) Non-dimensional amplitude $A$, (d-f) phase $\phi$, and (g-i) reflection coefficient $R^2$ versus cross-shore distance $x$ for tides 5 (black dots), 23 (circles) and 41 (grey dots) at Ameland. Left panels: $f$ = 0.011 Hz ($T$ = 90 s); middle panels: $f$ = 0.022 Hz ($T$ = 45 s); right panels: $f$ = 0.044 Hz ($T$ = 22.5 s). $A$ and $\phi$ were computed from the dominant Empirical Orthogonal Function of the cross-spectral matrix for each period. In the cases presented here, the dominant eigenfunction explained more than 90%-95% of the variance. The cross-spectra were computed from 900 s long, 50% overlapping, detrended, and Hamming-windowed series. The infragravity fluxes and $R^2$ were calculated with the array-method of Van Dongeren et al. (2007).

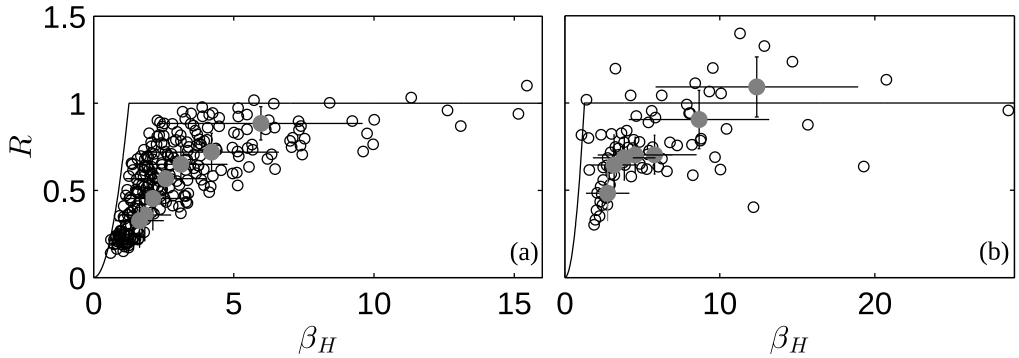


Figure 6: Amplitude reflection coefficient $R$ versus normalized bedslope $\beta_H$ at (a) P10 at Ameland and (b) PT8 at Egmond, The circles represent $f$ =0.011 Hz to $f$ = 0.044 Hz with a 0.0055 Hz step size. The grey dots are mean class values for the same frequencies, from $f$ = 0.044 Hz in the lower left to $f$ = 0.011 Hz in the upper middle part of the plot. The horizontal and vertical error bars are ± one standard deviation in $\beta_H$ and $R$, respectively. The solid line is $\min(1, R = 2\pi{\beta_H}^2)$ (Van Dongeren et al., 2007). The infragravity fluxes were calculated with the single-point method of Sheremet et al. (2002).

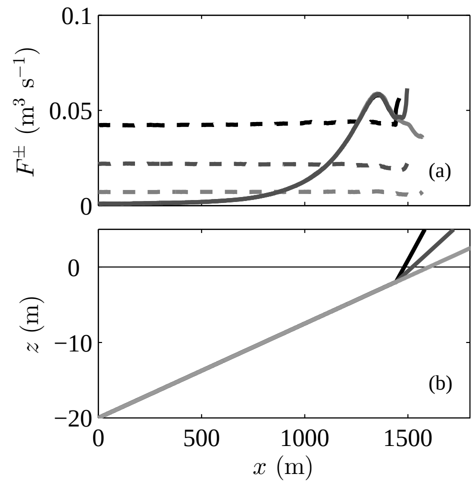


Figure 7: Model simulations for $H_0 = 2$ m, predicted (a) incoming (solid line) and outgoing (dashed line) infragravity-wave energy fluxes with $c_f = 0$. Panel (b) shows the three bed elevations $z$ versus $x$, (black) $\beta$ = 1:20, (grey) $\beta$ = 1:40 and (light grey) $\beta$ = 1:80.

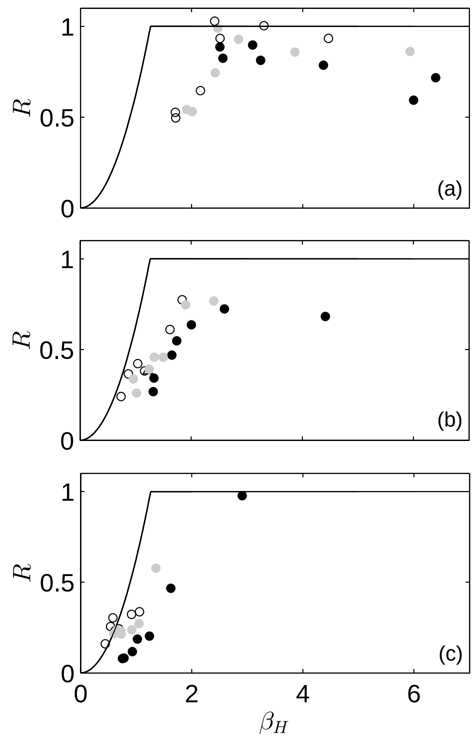


Figure 8: Amplitude reflection coefficient $R$ versus normalized bedslope $\beta_H$ for 1D SWASH-model simulations for (a) $\beta = 1{:}20$, (b) $\beta = 1{:}40$ and (c) $\beta = 1{:}80$. The datapoints represent $f = 0.011$ Hz to $f = 0.044$ Hz with a 0.0055 Hz step size for $H_0 = 1$ m (black dots), $H_0 = 2$ m (grey dots) and $H_0 = 3$ m (circles). The solid line is $\min(1, R = 2\pi {\beta_H}^2)$ (Van Dongeren et al., 2007). The infragravity fluxes were calculated with the single-point method of Sheremet et al. (2002). The scatter induced by the three offshore wave conditions might be due to the different cross-shore position of the last always wet point.

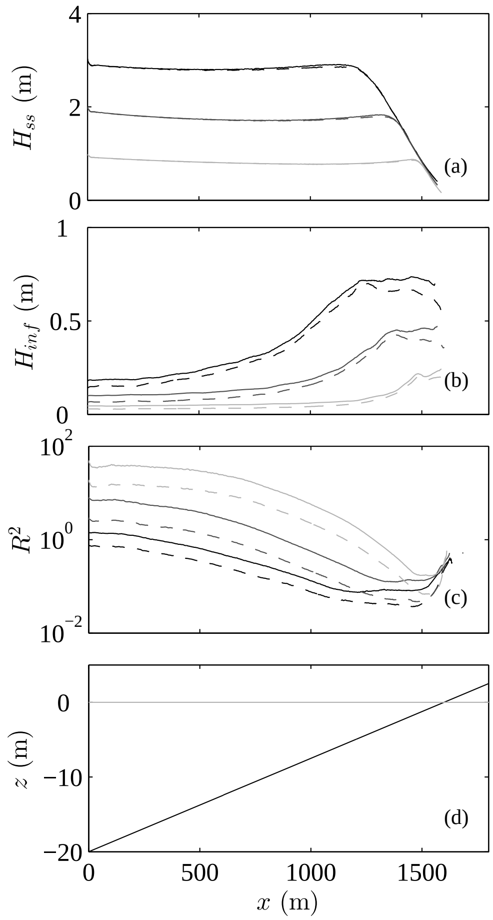


Figure 9: Predicted (a) short wave height $H_{ss}$, (b) infragravity wave height $H_{inf}$ and (c) bulk infragravity-wave reflection coefficients $R^2$ versus cross-shore distance $x$. Lines are (black) $H_0 = 1$ m, (grey) $H_0 = 2$ m and (light grey) $H_0 = 3$ m, with $c_f = 0$ (solid line) and $c_f = 0.005$ (dashed line). Panel (d) shows the bed elevation $z$ versus $x$.

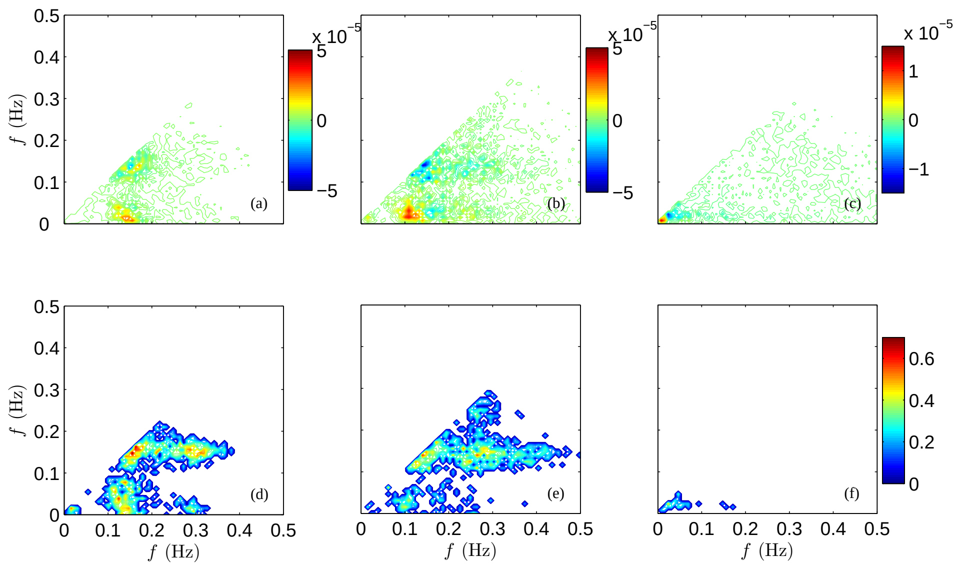


Figure 10: (a-c) Imaginary part of the bispectrum, (d-f) bicoherence values within the 95 % confidence interval ($b^2_{95\%} = 0.169$). Left panels: $x = 1000$ m (seaward of the surf zone); middle panels: $x = 1400$ m (mid surf zone); right panels: $x = 1540$ m (close to shore; shoreline is at 1574 m).

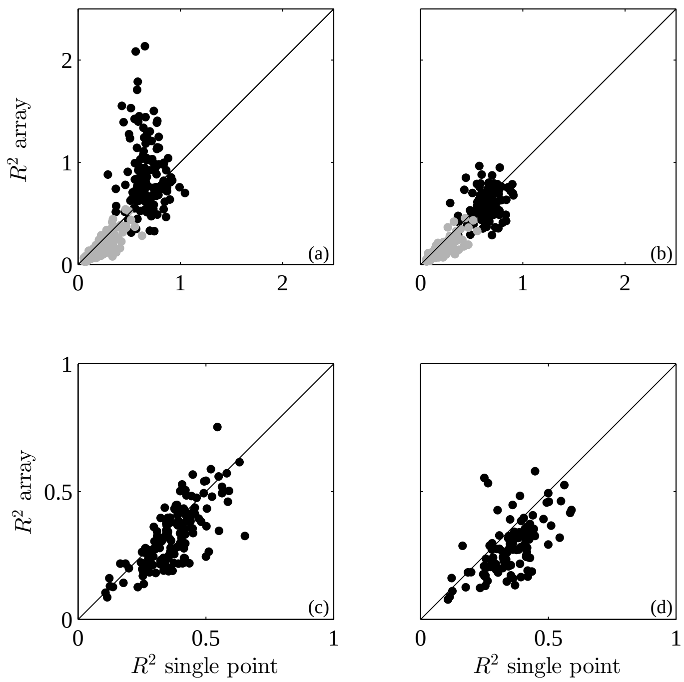


Figure A.1: Infragravity-wave reflection $R^2$ comparison for the Ameland data set. Array refers to the Van Dongeren et al. (2007)-method and single-point to the Sheremet et al. (2002)-method. (a and c) 3 sensors in the Van Dongeren et al. (2007)-method, (b and d) 5 sensors in the Van Dongeren et al. (2007)-method. (a and b) display the bulk infragravity $R^2$ divided into the 0.005-0.0167 Hz band (black dots) and the 0.0167-0.05 Hz band (grey dots). (c and d) display the bulk infragravity $R^2$ for the 0.005-0.05 Hz band.